Circuit Models and Fast Optimization of Litz Shield for Inductive-Power-Transfer Coils

Ming Lu, *Member, IEEE*, and Khai D. T. Ngo, *Fellow, IEEE*

***Abstract*—The metal shields with plates or rings are usually added to the inductive-power-transfer coils to attenuate the stray magnetic field. However, the coil-to-coil efficiency is reduced owning to the extra losses on the shields. This paper introduces the litz shield which attenuates the field with smaller shielding loss thanks to the uniform distribution of the shield current. Two types of litz shields, i.e., shorted litz shield and driven litz shield are discussed in detail. Their performances are analyzed with the circuit model composed of four coupled inductors. The efficiency and the field attenuation for the coils with litz shields are optimized with Pareto fronts. A fast method to derive the fronts using a lumped-loop model is described. Only tens of finite-element simulations are required in the entire optimization. The coils with different shields were optimized to transfer 100-W power across 40-mm gap with the same efficiency. The measurement results prove that the shorted litz shield is more effective than the other shields. It attenuated 23% more of the stray magnetic field compared to the coils with traditional metal shield.**

***Index Terms*—Coils, efficiency, inductive power transfer (IPT), litz wire, magnetic field, shields.**

I. Introduction

INDUCTIVE power transfer (IPT) to charge electric vehicles uses loosely coupled coils to replace the cables and plugs [1]–[4]. Planar coils are suitable for the applications that require mechanical simplicity and constrained depth, so they are commonly used in IPT. The design process of IPT coils for power transferability and efficiency has been demonstrated in literature [5]–[11].

Significant stray magnetic field exists around the IPT coils owning to the gap. It represents either leakage field or coupling field, depending on the distance from the measurement position to the coils [12]. The magnetic field $B(t)$ at the point of measurement is decomposed into $B_i(t)\,(i = X, Y, Z)$ in three orthogonal orientations, as shown in Fig. 1. $B_i(t)$ is sinusoidal because it is proportional to the winding currents which are roughly sinusoidal in IPT. The magnetic field $B(t)$ is quantified as

$$B = \sqrt{\sum\nolimits_{i=X,Y,Z} B_i^2} \tag{1}$$

where B_i is the RMS value of the sinusoidal $B_i(t)$.

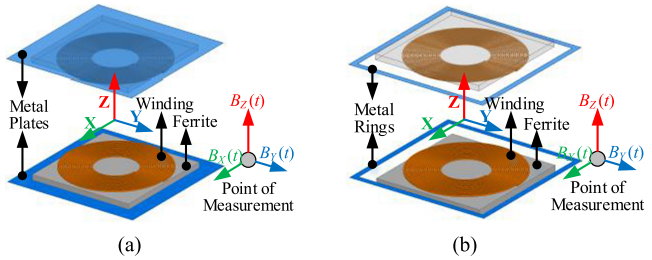

Fig. 1. (a) Plate shield and (b) ring shield to attenuate stray magnetic fields around coils.

International Commission on Non-Ionizing Radiation Protection reports that the effects such as the stimulation of nervous tissues and induction in the retina of phosphenes are caused by the exposure to time-varying magnetic field [13]. The ferrite plate in Fig. 1 is commonly used for field attenuation. The methods such as optimizing the size of ferrite plate [14], tuning the distribution of turns [15], or controlling the currents' phases in coils [16] can attenuate the stray magnetic field. However, the magnetic shield only is not good enough for high-power applications such as the charging of electric vehicles. Active shields or passive shields are always applied together with the magnetic shield.

Active shields are realized with shielding coils placed around the power-transfer coils. The stray magnetic fields penetrating the active shields are sensed to calculate the magnitudes and phases of the currents in the active shields. Using tunable capacitors is one way to actively control the shielding current [17]. Tunable capacitors which are realized by capacitor blocks and active switches are connected to the shielding coils. With the voltage across the shielding coils induced by the power-transfer coils, the shielding current is determined by the impedance of the shielding coils plus the tunable capacitance. Another method is to supply the shield current directly from an ac current source [18]. The shielding current flows in the opposite direction to the current in the power-transfer coils. The position and currents of the active shields are optimized according to the structure of the power-transfer coils. To make the active shields simpler to implement, another method is demonstrated in [19] to attenuate the stray magnetic field with the winding current in the

Manuscript received September 17, 2017; revised February 7, 2018 and May 9, 2018; accepted July 31, 2018. Date of publication August 14, 2018; date of current version March 29, 2019. This work was supported by the High Density Integration Consortium in the Center for Power Electronics Systems, Virginia Tech. Recommended for publication by Associate Editor C. R. Sullivan. *(Corresponding author: Ming Lu.)*

M. Lu is with Monolithic Power Systems Inc., San Jose, CA 95119 USA (e-mail:

power-transfer coils. The shielding coil is reversely connected to the power-transfer coil in series. The magnetic fields generated by the power-transfer coils and by the shielding coils attenuate each other on the side of the coils.

Passive shields are made of conductive materials which are placed around the IPT coils [20]–[25]. Different shapes of passive shields have been used for inductive-power-transfer coils. Fig. 1 shows two of the most commonly used passive shields with plate structure and ring structure. The plate shield implements the metal plate underneath the ferrite plate. The ring shield uses the metal ring on the side of the coils. When passive shields are added to IPT coils, the magnetic fields generated by the windings induce eddy currents in the shields. The directions of shield currents and winding currents are opposite, leading to reduced magnetic field around the coils. The dimensions and position of the passive shields should be optimized for field attenuation and efficiency. However, even with this optimization of dimensions and position, the shield current in Fig. 1 mostly flows on the surface owning to skin effect, which significantly increases the shielding losses. In order to overcome this problem, shields made of litz wires are used.

In this paper, two types of litz shields, shorted litz shield and driven litz shield, are discussed in detail. Shorted litz shield belongs to passive shield because the field is attenuated by the induced eddy current. The shielding turns of litz wire are self-shorted and disconnected from the windings. The driven litz shield is the same as the shield in [19] and belongs to active shields. Its shielding turns are connected to the windings in series, but in the reverse direction. The stray magnetic field is attenuated by the supplied current that flows in the shield. Both the induced eddy current in the shorted litz shield and the supplied current in the driven litz shield are evenly distributed, so the shielding losses are reduced. The circuit models with four coupled inductors are derived to analyze the performance of coils with litz shield. The windings' currents, shields' currents, equivalent inductances, and equivalent resistances are all calculated from the circuit models.

Pareto fronts are used to optimize the coil-to-coil efficiency and the stray magnetic field of litz shield. The fronts are plotted on a Cartesian coordinate system. The horizontal axis and vertical axis represent efficiency and magnetic field, respectively. One straightforward way to derive the Pareto fronts is to sweep the physical parameters of the windings and shields in finite-element simulation, such as the inner and outer radii of the windings, the dimensions of the shields, and the turns' distributions of the windings and shields. However, this takes thousands of simulations which are very time consuming. A faster method to derive the Pareto front is demonstrated in this paper, which will be explained in detail in Section III. In this method, the coils with litz shield are replaced with the lumped-loop model, in which the windings and shields are represented by several loops. It is called the lumped loop because each loop may contain several winding turns. Those physical parameters to sweep in the coils with litz shields are represented with the turns' numbers of the loops. As long as the number of turns for each lumped loop is known, the inductances and stray magnetic field can be calculated instead of being simulated. Then, the efficiency and magnetic field are derived accordingly. Therefore, sweeping physical parameters in finite-element simulation is replaced by sweeping turns numbers of lumped loops in calculation. Only tens of simulations are required in the entire optimization. This makes the optimization faster without losing the accuracy.

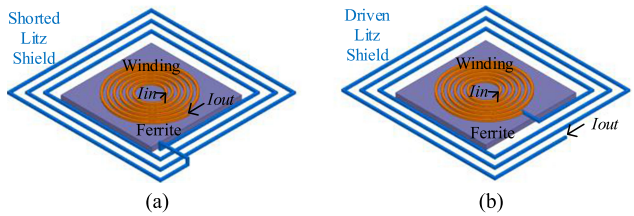

Fig. 2. Side view of coils with (a) shorted litz shield and (b) driven litz shield.

With the method of lumped-loop model, the Pareto fronts for the coils with litz shield are derived in this paper for an IPT system which transfers 100-W power across 40-mm gap. Pareto fronts of coils with metal shields are derived for comparison. The optimal designs of plate shield, ring shield, shorted litz shield, and driven litz shield are selected along the fronts for around 94.5% efficiency. The selected structures are fabricated and measured in experiment. The simulation and measurement results match well. The shorted litz shield is more effective than other shields. It attenuates the stray field by 65% compared to coils without metal shield, and attenuates the field by at least 23% more effective compared to the coils with other metal shields.

Section II demonstrates the structures and circuit models of the litz shield. Section III shows the calculation of stray magnetic field and efficiency using the lumped-loop model. Section IV summarizes the procedure of fast optimization with lumped-loop model and Pareto fronts. In Section V, the performances of coils with different shields were compared in experiment to transfer 100-W power across 40-mm gap with the same efficiency. Section VI concludes this paper.

II. Litz Shield for Inductive-Power-Transfer Coils and the Circuit Model

A. Structures of Litz Shield

The current of the metal shield in Fig. 1 flows in the opposite directions to the winding current, and this attenuates the stray magnetic field on the side of the coils. However, the current density is not uniformly distributed in the shield owning to skin effect. The current density is higher in the region that is closer to the winding because of the higher magnetic field. The uneven distribution of the current increases the shielding loss significantly.

The metal shields in Fig. 1 are replaced with the turns of litz wires, as shown in Fig. 2. The cross section of the litz shield is fully utilized with negligible skin effect, which reduces the shielding loss. The turns of shields are connected in series, so the shield currents are the same for all the turns. Fig. 2 shows two types of litz shields. The shorted litz shield in Fig. 2(a) is self-shorted, and it is disconnected from the winding. The eddy

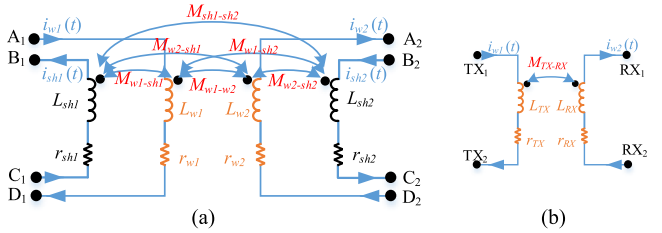

Fig. 3. (a) Circuit model of coils with litz shield and (b) its simplified circuit model. Calculations of the parameters are summarized in Fig. 9.

current induced on the shield attenuates the field on the side. The driven litz shield in Fig. 2(b) is connected to the winding in series, but in the reverse direction. The fields generated by the driven litz shield and by the winding have opposite directions on the side of the coil.

B. Circuit Model of Coils With Litz Shield

The litz shields in Fig. 2 behave like additional coils which are coupled with the windings. Fig. 3(a) shows the circuit model of the coils with litz shield. The windings of the transmitter and receiver are modeled as inductances L_{w1}, L_{w2} and equivalent series resistances (ESRs) r_{w1}, r_{w2}, whereas the shields are modeled as L_{sh1}, L_{sh2} and r_{sh1}, r_{sh2}. All of the four inductances are coupled between each other. $M_{w(j)-sh(i)}$ is the mutual inductance between the winding j and the litz shield i, with i or $j = 1$ representing the transmitter and i or $j = 2$ representing the receiver; M_{w1-w2} is the mutual inductance between the windings; and $M_{sh1-sh2}$ is the mutual inductance between the litz shields. The parameters can be extracted from simulation, or calculated with lumped-loop model in Section III.

The circuit model in Fig. 3(a) is simplified to the model in Fig. 3(b) with only two coupled inductors. In Fig. 3(b), the equivalent inductances L_{TX}, L_{RX}, and $M_{\mathrm{TX\text{-}RX}}$ and the equivalent resistances r_{TX} and r_{RX} are derived from Fig. 3(a). TX_1, TX_2, RX_1, and RX_2 are the terminals of the windings. The voltages between the terminals in Fig. 3(a) are derived according to KVL as

$$\begin{bmatrix} V_{A_1D_1} \\ V_{A_2D_2} \\ V_{B_1C_1} \\ V_{B_2C_2} \end{bmatrix} = j\omega \begin{bmatrix} L_{w1} & M_{w1-w2} & M_{w1-sh1} & M_{w1-sh2} \\ M_{w1-w2} & L_{w2} & M_{w2-sh1} & M_{w2-sh2} \\ M_{w1-sh1} & M_{w2-sh1} & L_{sh1} & M_{sh1-sh2} \\ M_{w1-sh2} & M_{w2-sh2} & M_{sh1-sh2} & L_{sh2} \end{bmatrix} \times \begin{bmatrix} I_{w1} \\ -I_{w2} \\ -I_{sh1} \\ I_{sh2} \end{bmatrix}. \tag{2}$$

For the coils with shorted litz shield in Fig. 2(a), B_1 and C_1 are connected, and B_2 and C_2 are connected. The terminals A_1, D_1, A_2, and D_2 in Fig. 3(a) are equivalent to the terminals TX_1, TX_2, RX_1, and RX_2 in Fig. 3(b), expressed as

$$\begin{bmatrix} V_{A_1D_1} & V_{A_2D_2} & V_{B_1C_1} & V_{B_2C_2} \end{bmatrix} = \begin{bmatrix} V_{\mathrm{TX_1TX_2}} & V_{\mathrm{RX_1RX_2}} & 0 & 0 \end{bmatrix}. \tag{3}$$

According to (2) and (3), the equivalent inductances L_{TX}, L_{RX}, and $M_{\mathrm{TX\text{-}RX}}$ and the equivalent resistances r_{TX} and r_{RX} in Fig. 3(b) are derived for the coils with shorted litz shield as

$$L_{\mathrm{TX}} = L_{w1} - \frac{M_{w1-sh2}^2}{L_{sh2}} - \frac{\left(L_{sh2}M_{w1-sh1} - M_{w1-sh2}M_{sh1-sh2}\right)^2}{L_{sh2}\left(L_{sh1}L_{sh2} - M_{sh1-sh2}^2\right)} \tag{4}$$

$$L_{\mathrm{RX}} = L_{w2} - \frac{M_{w2-sh1}^2}{L_{sh1}} - \frac{\left(L_{sh1}M_{w2-sh2} - M_{w2-sh1}M_{sh1-sh2}\right)^2}{L_{sh1}\left(L_{sh1}L_{sh2} - M_{sh1-sh2}^2\right)} \tag{5}$$

$$M_{\mathrm{TX-RX}} = M_{w1-w2} - \frac{L_{sh2}M_{w2-sh1} - M_{w2-sh2}M_{sh1-sh2}}{L_{sh1}L_{sh2} - M_{sh1sh2}^2}M_{w1-sh1} - \frac{L_{sh1}M_{w2-sh2} - M_{w2-sh1}M_{sh1-sh2}}{L_{sh1}L_{sh2} - M_{sh1-sh2}^2}M_{w1-sh2} \tag{6}$$

$$r_{\mathrm{TX}} = r_{w1} + \frac{\left(M_{sh1-sh2}M_{w1-sh2} - M_{w1-sh1}L_{sh2}\right)^2}{\left(L_{sh1}L_{sh2} - M_{sh1-sh2}^2\right)^2}r_{sh1} + \frac{\left(M_{sh1-sh2}M_{w1-sh1} - M_{w1-sh2}L_{sh1}\right)^2}{\left(L_{sh1}L_{sh2} - M_{sh1-sh2}^2\right)^2}r_{sh2} \tag{7}$$

$$r_{\mathrm{RX}} = r_{w2} + \frac{\left(M_{sh1-sh2}M_{w2-sh2} - M_{w2-sh1}L_{sh2}\right)^2}{\left(L_{sh1}L_{sh2} - M_{sh1-sh2}^2\right)^2}r_{sh1} + \frac{\left(M_{sh1-sh2}M_{w2-sh1} - M_{w2-sh2}L_{sh1}\right)^2}{\left(L_{sh1}L_{sh2} - M_{sh1-sh2}^2\right)^2}r_{sh2}. \tag{8}$$

For the coils with driven litz shield in Fig. 2(b), C_1 and C_2 are connected to D_1 and D_2, respectively. The terminals A_1, B_1, A_2, and B_2 in Fig. 3(a) are equivalent to the terminals TX_1, TX_2, RX_1, and RX_2 in Fig. 3(b) as

$$\begin{bmatrix} V_{A_1B_1} & V_{A_2B_2} & V_{C_1D_1} & V_{C_2D_2} \end{bmatrix} = \begin{bmatrix} V_{\mathrm{TX_1TX_2}} & V_{\mathrm{RX_1RX_2}} & 0 & 0 \end{bmatrix}. \tag{9}$$

According to (2) and (9), the equivalent inductances L_{TX}, L_{RX}, $M_{\mathrm{TX\text{-}RX}}$ and the equivalent resistances $r_{\mathrm{TX}}, r_{\mathrm{RX}}$ in Fig. 3(b) for the coils with driven litz shield are derived as

$$L_{\mathrm{TX}} = L_{w1} - L_{sh1} \tag{10}$$

$$L_{\mathrm{RX}} = L_{w2} - L_{sh2} \tag{11}$$

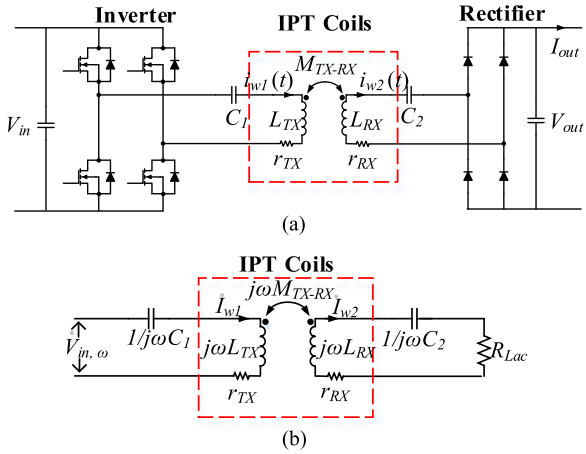

Fig. 4. (a) Circuit topology with series–series compensation for inductive power transfer and (b) its simplified circuit model.

$$M_{\mathrm{TX-RX}} = M_{w1-w2} - M_{sh1-sh2} + M_{w1-sh2} - M_{w2-sh1} \tag{12}$$

$$r_{\mathrm{TX}} = r_{w1} + r_{sh1} \tag{13}$$

$$r_{\mathrm{RX}} = r_{w2} + r_{sh2}. \tag{14}$$

The currents in the shields are derived from Fig. 3(a). The induced eddy currents in shorted litz shield are calculated as

$$i_{sh1}(t) = \frac{M_{w1-sh1}L_{sh2} + M_{w1-sh2}M_{sh1-sh2}}{L_{sh1}L_{sh2} + M_{sh1-sh2}^2} i_{w1}(t) - \frac{M_{w2-sh1}L_{sh2} + M_{w2-sh2}M_{sh1-sh2}}{L_{sh1}L_{sh2} + M_{sh1-sh2}^2} i_{w2}(t) \tag{15}$$

$$i_{sh2}(t) = \frac{M_{w1-sh2}L_{sh1} - M_{w1-sh1}M_{sh1-sh2}}{L_{sh1}L_{sh2} + M_{sh1-sh2}^2} i_{w1}(t) - \frac{M_{w2-sh2}L_{sh1} - M_{w2-sh1}M_{sh1-sh2}}{L_{sh1}L_{sh2} + M_{sh1-sh2}^2} i_{w2}(t) \tag{16}$$

where $i_{w1}(t)$ and $i_{w2}(t)$ are the winding currents of the transmitter and the receiver, respectively.

The currents in the driven litz shields are the same as the supplied currents in the windings as

$$i_{sh1}(t) = i_{w1}(t) \tag{17}$$

$$i_{sh2}(t) = i_{w2}(t). \tag{18}$$

The currents $i_{w1}(t)$, $i_{w2}(t)$, $i_{sh1}(t)$, and $i_{sh2}(t)$ are used to calculate the stray magnetic field, which is discussed in Section III.

C. Circuit Topology With Series–Series Compensation

Different topologies have been proposed to compensate the reactive power in inductive power transfer [26]–[31]. Fig. 4(a) shows the circuit topology with series–series compensation. In Fig. 4(a), V_{in}, V_{out}, and I_{out} are the input voltage, output voltage, and output current, respectively. The capacitors C_1 and C_2 are used to compensate the reactive power, and the resonant frequency of C_1 and L_{TX} is the same as that of C_2 and L_{RX}, expressed as

$$1/\sqrt{L_{\mathrm{TX}}C_1} = 1/\sqrt{L_{\mathrm{RX}}C_2} = 2\pi f_0. \tag{19}$$

The simplified circuit model in Fig. 4(b) is used to analyze the behavior of the circuit in Fig. 4(a). Under first-harmonic approximation, the dc input voltage V_{in} and the inverter are modeled as sinusoidal voltage source $\dot{V}_{\mathrm{in},\omega}$ in the format of phasor. The passive rectifier and the load are modeled as the equivalent resistor R_{Lac}. The phasors $\dot{I}_{\mathrm{TX}}$ and $\dot{I}_{\mathrm{RX}}$ are the currents of transmitter and receiver, respectively. The expressions of $\dot{V}_{\mathrm{in},\omega}$ and R_{Lac} are

$$\dot{V}_{\mathrm{in},\omega} = \left(2\sqrt{2}/\pi\right) V_{\mathrm{in}} \sin\left(\alpha/2\right) \angle 0^\circ \tag{20}$$

$$R_{Lac} = \left(8/\pi^2\right) \cdot \left(V_{\mathrm{out}}/I_{\mathrm{out}}\right) \tag{21}$$

where α is the pulsewidth of the inverter's output voltage, which is used to regulate the bulk power transferred to the load by controlling the phase shift between phase legs. Equations (22) and (23) are derived from the simplified circuit model in Fig. 4(b) with KVL

$$\dot{V}_{\mathrm{in},\omega} = \left[r_{\mathrm{TX}} + j \cdot \left(\omega_s L_{\mathrm{TX}} - 1/\omega_s C_1\right)\right] \dot{I}_{w1} - j \cdot \omega_s M \cdot \dot{I}_{w2} \tag{22}$$

$$0 = j \cdot \omega_s M \cdot \dot{I}_{\mathrm{TX}} - \left[r_{\mathrm{RX}} + R_{Lac} + j \cdot \left(\omega_s L_{\mathrm{RX}} - 1/\omega_s C_2\right)\right] \dot{I}_{\mathrm{RX}}. \tag{23}$$

In order to reduce the circulating energy in the circuit, the inverter's switching frequency equals the resonant frequency of C_1 and L_{TX}. In this case, the coil-to-coil efficiency, which is defined as the ratio of the receiver's output power to the transmitter's input power, is derived from (22) and (23) as

$$\eta_{\mathrm{coil}} = 1/\left[1 + \frac{r_{\mathrm{RX}}}{R_{Lac}} + \frac{r_{\mathrm{TX}}}{R_{Lac}} \cdot \frac{\left(r_{\mathrm{RX}} + R_{Lac}\right)^2}{\left(\omega_s M_{\mathrm{TX-RX}}\right)^2}\right]. \tag{24}$$

The windings' currents $i_{w1}(t)$ and $i_{w2}(t)$, which are used to calculate the shielding currents in (15)–(18), are calculated from the equivalent circuit model in Fig. 4(b) as

$$i_{w1}(t) = \left[\left(\pi R_{Lac}\right)/\left(2\omega_s M_{\mathrm{TX-RX}}\right)\right] I_{\mathrm{out}} \sin(\omega_s t) \tag{25}$$

$$i_{w2}(t) = \left(\pi/2\right) I_{\mathrm{out}} \sin(\omega_s t + \pi/2). \tag{26}$$

Fig. 5(a) shows a set of coils with litz shield as an example. The dimensions are labeled in the figure. There are 25 turns for each winding, and the total number of turns for the litz shield is swept from 1 to 8. The length of the square shield is fixed to be 130 mm, so the spacing between the shield and winding decreases with the shield's turns number increasing. The litz wire consists of 100 strands of AWG number 38 wires. Fig. 5(b) and (c) shows the equivalent mutual inductances and resistances versus turns number of litz shield. The inductances decrease and the resistances increase with the shields added. Fig. 5(d) shows the coil-to-coil efficiency, which is calculated from (24). The efficiency is reduced because of the shields, so the optimization of efficiency and field attenuation is necessary.

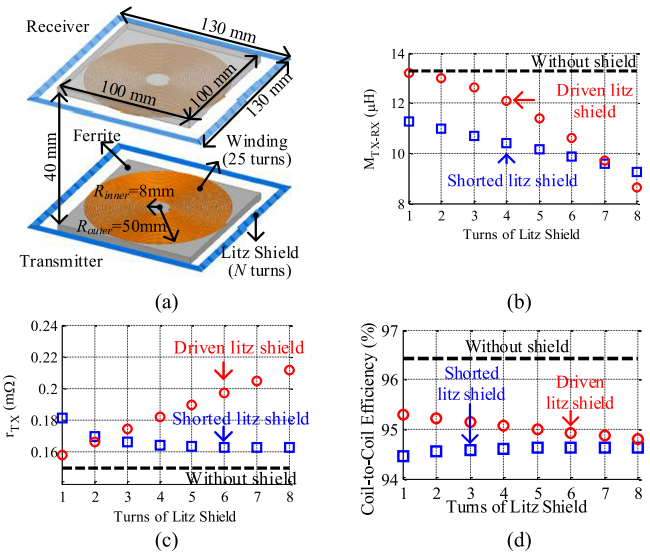

Fig. 5. (a) Structure of coils with litz shield as an example. (b) Equivalent mutual inductances. (c) Equivalent resistances. (d) Coil-to-coil efficiency calculated for coils without shield and with litz shield versus numbers of turns.

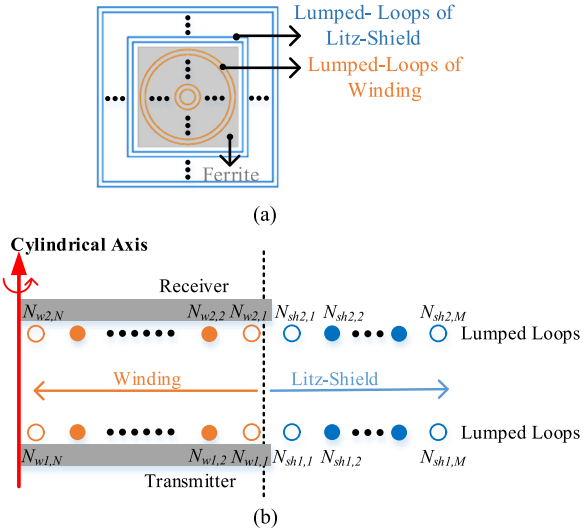

Fig. 6. (a) Top view and (b) side view of the lumped-loop model of IPT coils with litz shield. The turns vectors are $[N_{w1,1}, N_{w1,2}, \ldots, N_{w1,N}]$ and $[N_{w2,1}, N_{w2,2}, \ldots, N_{w2,N}]$ for the windings, and $[N_{sh1,1}, N_{sh1,2}, \ldots, N_{sh1,M}]$ and $[N_{sh2,1}, N_{sh2,2}, \ldots, N_{sh2,M}]$ for the litz shields. Distribution of turns is represented by turns vectors.

III. Lumped-Loop Model of Coils With Litz Shield

The inductances and resistances in Fig. 3(a) can either be derived from finite-element simulation or be calculated with lumped-loop model. When optimizing the litz shield, the physical parameters are swept. Simulating each case is too time consuming for the optimization. The calculation with lumped-loop model is more suitable for the optimization purpose, and this section will describe the lumped-loop model in detail.

A. Lumped-Loop Model and Turns Vectors

Fig. 6 shows the lumped-loop model of coils with litz shield. The winding and litz shield are replaced by several loops that are distributed on top of the ferrite plate with equal spacing. Each loop is composed of certain turns. Turns vectors $\vec{N}_{w1}$ and $\vec{N}_{w2}$ describe the turns numbers for the loops of the transmitter and receiver, respectively,

$$\vec{N}_{w1} = \left[N_{w1,1}\ N_{w1,2}\ \cdots\ N_{w1,N} \right] \tag{27}$$

$$\vec{N}_{w2} = \left[N_{w2,1}\ N_{w2,2}\ \cdots\ N_{w2,N} \right] \tag{28}$$

where $N_{w1,(n)}$ and $N_{w2,(n)}$ represent the turns number of loop n in the transmitter and receiver, respectively, with $n = 1, 2, \ldots, N$. Loop 1 represents the outermost loop, and loop N represents the innermost loop of the windings in Fig. 6(b).

The turns vectors $\vec{N}_{sh1}$ and $\vec{N}_{sh2}$ describe the number of turns for each loop of the litz shields in the transmitter and receiver, respectively,

$$\vec{N}_{sh1} = \left[N_{sh1,1}\ N_{sh1,2}\ \cdots\ N_{sh1,M} \right] \tag{29}$$

$$\vec{N}_{sh2} = \left[N_{sh2,1}\ N_{sh2,2}\ \cdots\ N_{sh2,M} \right] \tag{30}$$

where $N_{sh1,(n)}$ and $N_{sh2(n)}$ represent the turns number of loop n in litz shields of transmitter and receiver, respectively, with $n = 1, 2, \ldots, M$. Loop 1 represents the loop that is most close to the winding, whereas loop M represents the outermost loop of the litz shield in Fig. 6(b).

The purpose of using two-dimensional (2-D) axial symmetrical structure in Fig. 6(b) is to better explain the lumped-loop model and to label the elements of turns vector. The concept of the lumped-loop model and the optimization methodology are good for planar winding with different ferrite shapes (e.g., circular, square, or rectangular). For example, for the lumped-loop model in Fig. 6, the windings and shields are replaced by lumped loops, and the square ferrite plate is not changed. Three-dimensional (3-D) finite-element simulations in Ansys Maxwell are implemented to derive the permeance matrices and current-to-field matrices for the lumped loops model, which will be demonstrated in the following section.

The physical parameters of the coils are equivalent to the turns vectors in (27)–(30). In Fig. 6(b), the loops shown as hollow circles are assigned zero turn to realize the values of R_{inner}, R_{outer}, the length of the square shield, and the spacing between the winding and shield. The numbers of turns for the loops shown as solid circles represent the distribution of turns. Therefore, with the lumped-loop model and turns vectors, sweeping the physical parameters for the original coils such as Fig. 5(a) is equivalent to sweeping the turns vectors in (27)–(30) for the lumped-loop model in Fig. 6.

B. Inductances With Permeance Matrices

The lumped-loop model in Fig. 6 includes four parts: the windings and shields of transmitter and receiver. The permeance matrices in Fig. 7 are used to calculate the inductances in Fig. 3(a), together with turns vectors.

The permeance matrices $\mathbf{L_{w(i)}}$ and $\mathbf{L_{sh(i)}}$ are used to calculate the self-inductances of winding i and litz shield i, with $i = 1$

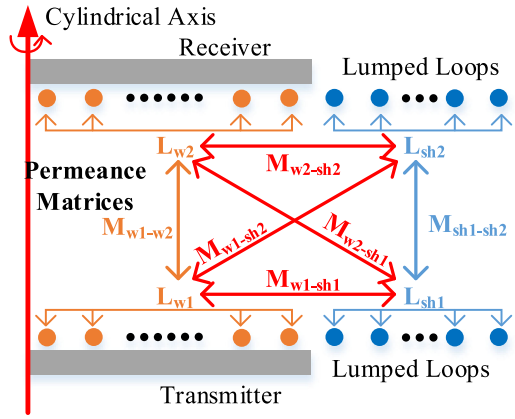

Fig. 7. Permeance matrices $\mathbf{L_{w1}}$, $\mathbf{L_{w2}}$, $\mathbf{L_{sh1}}$, $\mathbf{L_{sh2}}$, $\mathbf{M_{w1-w2}}$, $\mathbf{M_{sh1-sh2}}$, $\mathbf{M_{w1-sh1}}$, $\mathbf{M_{w1-sh2}}$, $\mathbf{M_{w2-sh1}}$, and $\mathbf{M_{w2-sh2}}$ of the lumped-loop model.

representing the transmitter and $i = 2$ representing the receiver

$$\mathbf{L_{w(i)}} = \begin{bmatrix} L_{w(i),1} & M_{w(i),1-w(i),2} & \cdots & M_{w(i),1-w(i),N} \\ M_{w(i),2-w(i),1} & L_{w(i),2} & \cdots & M_{w(i),2-w(i),N} \\ \vdots & \vdots & \ddots & \vdots \\ M_{w(i),N-w(i),1} & M_{w(i),N-w(i),2} & \cdots & L_{w(i),N} \end{bmatrix} \tag{31}$$

$$\mathbf{L_{sh(i)}} = \begin{bmatrix} L_{sh(i),1} & M_{sh(i),1-sh(i),2} & \cdots & M_{sh(i),1-sh(i),M} \\ M_{sh(i),2-sh(i),1} & L_{sh(i),2} & \cdots & M_{sh(i),2-sh(i),M} \\ \vdots & \vdots & \ddots & \vdots \\ M_{sh(i),M-sh(i),1} & M_{sh(i),M-sh(i),2} & \cdots & L_{sh(i),M} \end{bmatrix} \tag{32}$$

where $L_{w(i),n}$ and $L_{sh(i),n}$ are the self-inductances of loop n in the winding and litz shield, respectively; $M_{w(i),n-w(i),m}$ is the mutual inductance between loops n and m of the windings; and $M_{sh(i),n-sh(i),m}$ is the mutual inductance between loops n and m of the litz shields.

The permeance matrices $\mathbf{M_{w1-w2}}$, $\mathbf{M_{sh1-sh2}}$, $\mathbf{M_{w1-sh1}}$, $\mathbf{M_{w1-sh2}}$, $\mathbf{M_{w2-sh1}}$, and $\mathbf{M_{w2-sh2}}$ are used to calculate the mutual inductances among the four parts

$$\mathbf{M_{w1-w2}} = \begin{bmatrix} M_{w1,1-w2,1} & M_{w1,1-w2,2} & \cdots & M_{w1,1-w2,N} \\ M_{w1,2-w2,1} & M_{w1,2-w2,2} & \cdots & M_{w1,2-w2,N} \\ \vdots & \vdots & \ddots & \vdots \\ M_{w1,N-w2,1} & M_{w1,N-w2,2} & \cdots & M_{w1,N-w2,N} \end{bmatrix} \tag{33}$$

$$\mathbf{M_{sh1-sh2}} = \begin{bmatrix} M_{sh1,1-sh2,1} & M_{sh1,1-sh2,2} & \cdots & M_{sh1,1-sh2,M} \\ M_{sh1,2-sh2,1} & M_{sh1,2-sh2,2} & \cdots & M_{sh1,2-sh2,M} \\ \vdots & \vdots & \ddots & \vdots \\ M_{sh1,M-sh2,1} & M_{sh1,M-sh2,2} & \cdots & M_{sh1,M-sh2,M} \end{bmatrix} \tag{34}$$

$$\mathbf{M_{w(i)-sh(j)}} = \begin{bmatrix} M_{w(i),1-sh(j),1} & M_{w(i),1-sh(j),2} & \cdots & M_{w(i),1-sh(j),M} \\ M_{w(i),2-sh(j),1} & M_{w(i),2-sh(j),2} & \cdots & M_{w(i),2-sh(j),M} \\ \vdots & \vdots & \ddots & \vdots \\ M_{w(i),N-sh(j),1} & M_{w(i),N-sh(j),2} & \cdots & M_{w(i),N-sh(j),M} \end{bmatrix} \tag{35}$$

where $M_{w1,n-w2,m}$ is the mutual inductance between loops n of transmitter winding and loop m of receiver winding; $M_{sh1,n-sh2,m}$ is the mutual inductance between loops n of transmitter shield and loop m of receiver shield; and $M_{w(i),n-sh(j),m}$ is the mutual inductance between loops n of the winding i and loop m of the shield j, with i or $j = 1$ representing the transmitter and i or $j = 2$ representing the receiver.

All the elements of the permeance matrices in (31)–(35) are derived from one finite-element simulation with the lumped-loop model in Fig. 7, by setting single turn for each loop. The inductances of the circuit models in Fig. 3(a) are calculated from the permeance matrices and turns vectors as

$$L_{w(i)} = \vec{N}_{w(i)} \mathbf{L_{w(i)}} \vec{N}_{w(i)}^{\,T} \tag{36}$$

$$L_{sh(i)} = \vec{N}_{sh(i)} \mathbf{L_{sh(i)}} \vec{N}_{sh(i)}^{\,T} \tag{37}$$

$$M_{w1-w2} = \vec{N}_{w1} \mathbf{M_{w1-w2}} \vec{N}_{w2}^{\,T} \tag{38}$$

$$M_{sh1-sh2} = \vec{N}_{sh1} \mathbf{M_{sh1-sh2}} \vec{N}_{sh2}^{\,T} \tag{39}$$

$$M_{w(i)-sh(j)} = \vec{N}_{w(i)} \mathbf{M_{w(i)-sh(j)}} \vec{N}_{sh(j)}^{\,T}. \tag{40}$$

C. Stray Magnetic Field With Current-to-Field Matrices

The stray magnetic fields are calculated from the currents of the windings and the shields, using the current-to-field matrices. Similar concept has been described in [15] and [32]. According to superposition, the magnetic field $B_i(t)$ at the point of measurement in Fig. 8 is calculated from the summation of the fields generated by each loop

$$\begin{aligned} B_i(t) = &\sum_{n=1}^{N} \alpha_{w1,n,i} N_{w1,n} i_{w1}(t) + \sum_{n=1}^{N} \alpha_{w2,n,i} N_{w2,n} i_{w2}(t) \\ &+ \sum_{n=1}^{M} \alpha_{sh1,n,i} N_{sh1,n} i_{sh1}(t) \\ &+ \sum_{n=1}^{M} \alpha_{sh2,n,i} N_{sh2,n} i_{sh2}(t) \end{aligned} \tag{41}$$

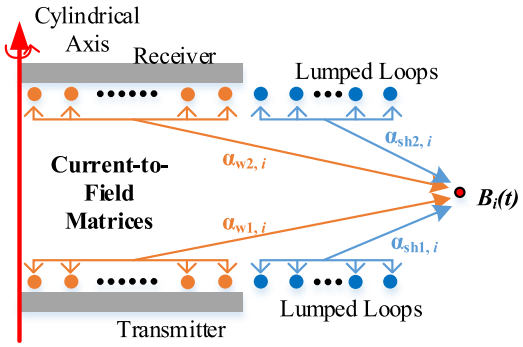

Fig. 8. Current-to-field matrices $\boldsymbol{\alpha}_{\mathbf{w1,i}}$, $\boldsymbol{\alpha}_{\mathbf{w2,i}}$, $\boldsymbol{\alpha}_{\mathbf{sh1,i}}$, and $\boldsymbol{\alpha}_{\mathbf{sh2,i}}$ of the lumped-loop model.

where $\alpha_{w(j),n,i}$ and $\alpha_{sh(j),n,i}$ are the current-to-field coefficients for loop n of winding j and shield j, respectively, with $j = 1$ representing the transmitter and $j = 2$ representing the receiver; i represents the orientations X, Y, or Z in Fig. 1(b); $N_{w(j),n}$ and $N_{sh(j),n}$ are the numbers of turns for the corresponding loop, which are the elements of the turns vectors in (27)–(30); and $i_{w(j)}(t)$ and $i_{sh(j)}(t)$ are the currents of winding j and litz shield j, respectively.

The current-to-field matrices $\boldsymbol{\alpha}_{\mathbf{w1,i}}$, $\boldsymbol{\alpha}_{\mathbf{w2,i}}$, $\boldsymbol{\alpha}_{\mathbf{sh1,i}}$, and $\boldsymbol{\alpha}_{\mathbf{sh2,i}}$ are composed of the current-to-field coefficients in (41)

$$\boldsymbol{\alpha}_{\mathbf{w(j),i}} = \left[\alpha_{w(j),1,i}\ \alpha_{w(j),2,i}\ \cdots\ \alpha_{w(j),N,i}\right] \tag{42}$$

$$\boldsymbol{\alpha}_{\mathbf{sh(j),i}} = \left[\alpha_{sh(j),1,i}\ \alpha_{sh(j),2,i}\ \cdots\ \alpha_{sh(j),M,i}\right]. \tag{43}$$

The current-to-field coefficients of one loop is derived by setting 1 ampere-turn in this loop and setting 0 ampere-turn to all the others. If there are N loops for the winding and M loops for the shield in both transmitter and receiver, $2(N + M)$ simulations are required to derive all the elements in the current-to-field matrices. After the current-to-field matrices in (42) and (43) are derived, the stray magnetic fields in X, Y, Z orientations are calculated from (41) with turns vectors in (27)–(30), winding currents in (25) and (26), and shielding currents in (15)–(18).

D. Coil-to-Coil Efficiency

According to (24), the coil-to-coil efficiency is determined by r_{TX} and r_{RX}, which are calculated from r_{w1}, r_{w2}, r_{sh1}, and r_{sh2} in Fig. 3(a) using (7), (8), (13), and (14). The winding resistance r_{w1} includes the dc resistance of transmitter winding, the proximity-effect resistance of transmitter winding, and the reflected proximity-effect resistance of the transmitter shield. The shield resistances r_{sh1} represents the dc resistances of the transmitter shield. The definitions of r_{w2} and r_{sh2} for the receiver are similar to r_{w1} and r_{sh1}. The skin-effect resistances are negligible when the strand diameter is selected to be much smaller than the skin depth. Litz wire with proper strand diameter is utilized for the windings in all the cases studied in this paper.

The dc resistances are calculated from the physical parameters of the litz wire (e.g., the cross-sectional area and length). The proximity-effect resistance can be calculated following the methods in [33]–[37]. The method in [34] is applied in this paper

$$P_{e,n} = \left[\left(\pi l_{t,n} N d_c^4\right)/(64\rho_c)\right] \cdot \left\langle \overline{(dB(t)/dt)^2} \right\rangle \tag{44}$$

where $P_{e,n}$ is the proximity-effect loss of turn n for either the winding or the shield; $l_{t,n}$ is the average length of the turn; N is the number of strands; d_c is the diameter of the strand; ρ_c is the resistivity of copper; $B(t)$ is the time-varying flux density across the turn; $\langle x \rangle$ is the spatial average over the turn's cross section; and $\bar{x}$ is the time average.

The proximity-effect loss of the transmitter is mainly caused by the transmitter itself. The receiver contributes a negligible portion of the proximity-effect loss on the transmitter. It is the same for the receiver. This is because the proximity-effect loss is caused by the magnetic field penetrating the turns, and the majority of the magnetic field penetrating the turns of the transmitter is generated by the transmitter itself.

The proximity-effect resistance r_{e1} of the transmitter is calculated from the total proximity-effect loss of the winding turns and shielding turns

$$r_{e1} = \sum_{n=1}^{N_{\mathrm{turns}}} P_{e,n}/I_{w1}^2 \tag{45}$$

where I_{w1} is the RMS value of winding current. The proximity-effect resistance of the receiver r_{e2} is calculated similarly.

To analytically calculate the magnetic fields across the turns in (44), the lumped-loop model is translated back to the original coils with real turns according to the turns vectors. The magnetic field across each turn is then analytically calculated using the methods in [35].

IV. Fast Optimization of Coils With Litz Shield

The coils' efficiency is reduced after the shields are added. The optimization of the efficiency and stray magnetic field is herein realized with Pareto fronts for the coils with litz shield. The fronts are plotted on a 2-D Cartesian coordinate system. The horizontal axis and vertical axis represent the magnetic field and coil-to-coil efficiency, respectively. The optimal designs of the coils are selected along the fronts [12].

The straightforward method to derive Pareto fronts is by sweeping the physical parameters in finite-element simulation. The efficiency and stray magnetic field are then obtained for each case from the simulation results. Taking the coils structures in Fig. 5(a) as an example, the circular winding is placed above the ferrite plate and the litz shield is placed around the ferrite plate. The swept physical parameters include R_{inner}, R_{outer}, the length of the square shield, the spacing between winding and shield, and the distributions and types of the litz wires. The parametric sweep takes thousands of simulations, which is very time consuming especially for 3-D models. Therefore, the efficiency and magnetic field should be calculated for each case instead of being simulated, in order to make the optimization faster. This is realized with the lumped-loop model, following the procedure in Fig. 9.

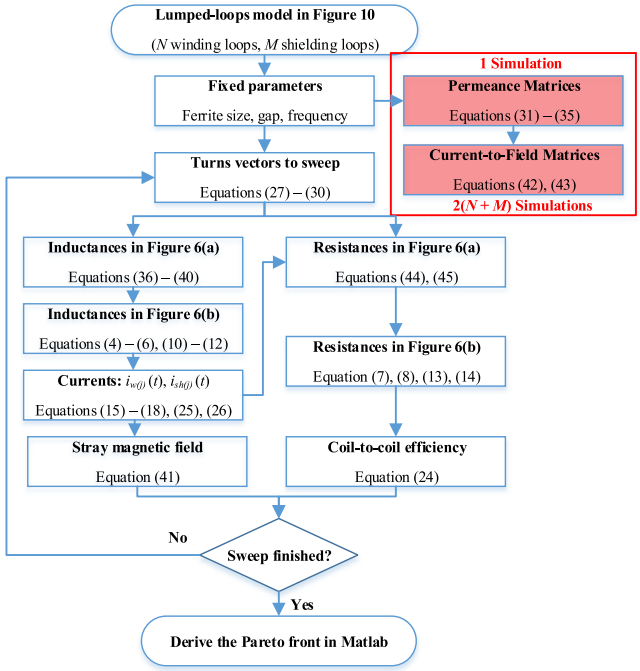

Fig. 9. Procedures to derive the Pareto front of coil-to-coil efficiency versus stray magnetic field from calculation with lumped-loop model.

In Fig. 9, one simulation is required to derive the permeance matrices in (31)–(35), and tens of simulations are implemented to obtain the current-to-field matrices in (42) and (43).

The procedure starts off by selecting the lumped-loop model with some fixed parameters, such as the size of ferrite, the air gap, and the frequency. The turns vectors in (27)–(30) are swept to represent the physical parameters, such as the R_{inner}, R_{outer}, length, and the spacing between the winding and shield. The domain of the represented R_{outer} and R_{inner} can be selected to avoid unnecessary cases that are obvious far away from optimal solutions. For example, if R_{outer} is considerably smaller than ferrite side, more turns of thinner wires are required to realize the desired inductance, resulting in extremely low efficiency. During the optimization procedure in this paper, the domain of R_{outer} is selected to be (ferrite side/10) $\leq R_{\text{outer}} \leq$ (ferrite side/2), and the domain of R_{inner} is selected to be $0 < R_{\text{inner}} \leq R_{\text{outer}}$, respectively.

For each set of turns vectors, the stray magnetic field and coil-to-coil efficiency are calculated following the method in Section III. The stray magnetic fields are derived from (41), with the current-to-field matrices, the shields currents, the winding currents, and the turns vectors. The shields currents $i_{sh1}(t)$ and $i_{sh2}(t)$ are calculated from (15)–(18) with the inductances in Fig. 3(a). The winding currents $i_{w1}(t)$ and $i_{w2}(t)$ are calculated from (25) and (26) with the inductances in Fig. 3(b). The inductances in Fig. 3(a) are derived from the permeance matrices in (36)–(40), and the inductances in Fig. 3(b) are derived from (4)–(6) and (10)–(12).

The coil-to-coil efficiency is calculated from (24), with r_{TX} and r_{RX} in Fig. 3(b). The equivalent resistances r_{TX} and r_{RX} are calculated from (7), (8), (13), (14) with the resistances r_{w1}, r_{w2}, r_{sh1}, and r_{sh2} in Fig. 3(a). The resistances include dc resistances and proximity-effect resistances. The dc resistance is calculated from the physical parameters of the coils, and the proximity-effect resistances are calculated from (44) and (45).

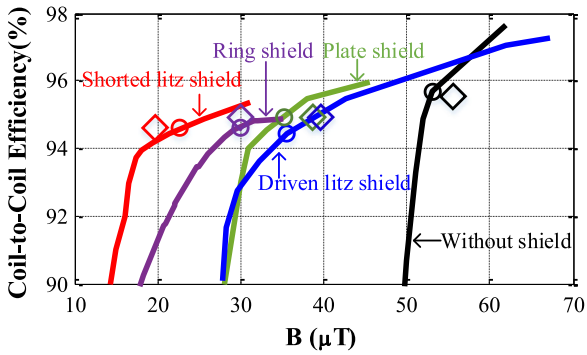

Fig. 10. Pareto fronts of coil-to-coil efficiency versus stray magnetic field for coils with no shield, plate shield, ring shield, shorted litz shield, and driven litz shield. Horizontal axis is the stray magnetic field at point (0, 100 mm, 0) in Fig. 1(b), with 100-W power transferred across 40-mm gap.

After the coil-to-coil efficiencies and stray magnetic fields for all the turns vectors are calculated, the Pareto fronts are derived in MATLAB and plotted on the Cartesian coordinate system. Fig. 10 shows the Pareto fronts derived following the procedure in Fig. 9, for the coils structures in Fig. 5(a) with shorted litz shield and driven litz shield. The power of 100 W is transferred across 40-mm gap, with 35-V output voltage and 100-kHz switching frequency. The square ferrite plate has the dimensions of 100 mm $\times$ 100 mm $\times$ 5 mm with 3C96 material. The magnetic field is optimized at the point (0, 100 mm, 0) in Fig. 1. The origin is the center between transmitter and receiver.

The Pareto fronts for coils without shields, with plate shield, and with ring shield are plotted in Fig. 10 for comparison. During the optimization of the plate shield and ring shield, the size and position of the plate, the width and position of the flat ring were swept in finite-element simulation. The efficiency is reduced with shields, but the stray magnetic field is significantly attenuated. The shorted litz shield attenuates the field most when the four shields are designed for the same efficiency. Compared to the plate shield and ring shield, the skin effect in shorted litz shield is negligible so the shield current is higher for the same amount of losses. Higher current in the shields helps us to attenuate the stray magnetic field more. The performance of the shorted litz shield is better than that of the driven litz shield. This is because the current of the driven litz shield is limited to the supplied value, while the induced eddy current in shorted litz shield is able to adjust according to the magnetic field.

V. Experimental Verification

The circles along the Pareto fronts in Fig. 10 represent the optimal coils with different shields, and they have similar efficiency around 94.5%. The coils corresponding to the circles were fabricated for experimental test, as shown in Fig. 11. The litz wires used for all the structures in Fig. 11 are composed of 100 AWG #38 strands with 100-μm strand diameter. This strand diameter is a reasonable choice for 100-kHz operation when the

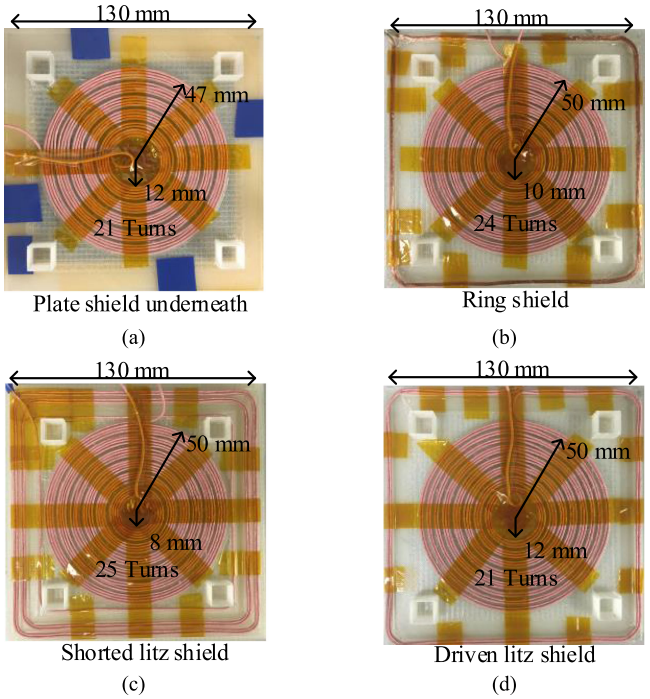

Fig. 11. Fabricated coils for the selected structures marked as circles along the Pareto fronts in Fig. 10 with (a) plate shield, (b) ring shield, (c) shorted litz shield, and (d) driven litz shield. The coils are optimized to transfer 100-W power across 40-mm gap.

TABLE I
MEASURMENT RESULTS FOR COILS IN FIG. 11

Parameters	L_{TX}, L_{RX} (μH)	$M_{TX\text{-}RX}$ (μH)	r_{TX}, r_{RX} at 100 kHz (mΩ)	Coil Efficiency (%)
No Shield	36	8.7	106	95.7
Plate shield	40	8.8	125	94.7
Ring shield	49	11	175	94.7
Shorted litz shield	45	9.8	160	94.4
Driven litz shield	44	9.6	145	94.7

skin depth is 206 μm. Even though it cannot completely eliminate the skin effect, it makes the skin-effect loss negligible. The dc resistance is more dominating at 100 kHz than ac resistance for the coils in Fig. 11. The ac resistance is less than 20% of the total resistance.

The measurement results of the inductances and resistances for the coils in Fig. 11 are listed in Table I. They were measured in the presence of both transmitter and receiver coils with a 40-mm air gap. Impedance analyzer Agilent 4294 A was used for the measurement. The switching frequency is 100 kHz for the IPT circuit in the experiment and the ac resistances at 100 kHz are given in Table I. When the resistance of one coil was measured, the other coil was open. The coil-to-coil efficiencies are calculated from (24) with the mutual inductances and resistances. The weight breakdown of the coils is listed in Table II. The increase of weight for ring shield and litz shields is negligible, while the plate shield almost doubles the total weight.

TABLE II
WEIGHT BREAKDOWN FOR TRANSMITTER COIL IN FIG. 11
(FERRITE WEIGHT = 240 g)

Parameters	Winding Weight (g)	Shield Weight(g)
No Shield	28	0
Plate shield	31	192
Ring shield	35	14
Shorted litz shield	36	19
Driven litz shield	32	4

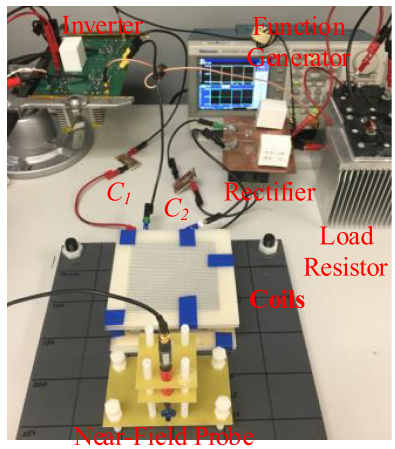

Fig. 12. Hardware setup for field measurement of the coils in Fig. 11.

The hardware for field measurement is shown in Fig. 12. The near-field probe Langer EMV LF-R 50 was used to measure $B_X(t)$, $B_Y(t)$, and $B_Z(t)$ at each point. Fig. 13 shows the measured waveforms of $B_Y(t)$ and $B_Z(t)$ at the point (0, 100 mm, 0) in Fig. 1, for the coils without shield and with the shields in Fig. 11. The power of 100 W was transferred from the transmitter to receiver across 40-mm gap. The field in the *X*-direction is negligible due to the symmetry, so it is not plotted. The comparison in Fig. 13 proves that the shorted litz shield attenuates the field more than other shields on both *Y*- and *Z*-directions.

The measurement results of the coil-to-coil efficiency in Table I and the stray magnetic fields for the coils in Fig. 11 are plotted as diamonds in Fig. 10. The magnetic fields were quantified with (1). The diamonds match well with the circles which are the calculation results. The errors are mostly caused by the deviations of coils' fabrication and probe's position. Shorted litz shield with 94.4% efficiency attenuates the stray field by 65% compared to coils without shield whose efficiency is 95.7%.

Moreover, the optimal design of the shorted litz shield is usually composed of only a few turns of shield, because too many turns increase the shielding loss. The shield should not be too close to the ferrite plate, to avoid inducing too much eddy current on the shield which will reduce the efficiency significantly.

Although the shields were optimized for the magnetic field at the point (0, 100 mm, 0), the stray magnetic fields at other positions are attenuated as well. Fig. 14 shows the quantified results of the measured fields on the side of the coils along the

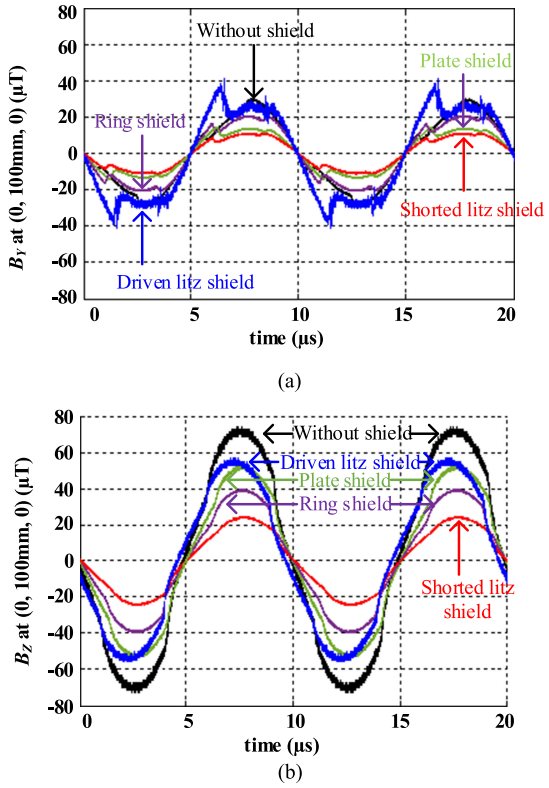

Fig. 13. Comparison of $B_Y(t)$ and $B_Z(t)$ at point (0, 100 mm, 0) for coils without and with shields. The stray magnetic fields were measured with 100-W power transferred across 40-mm gap.

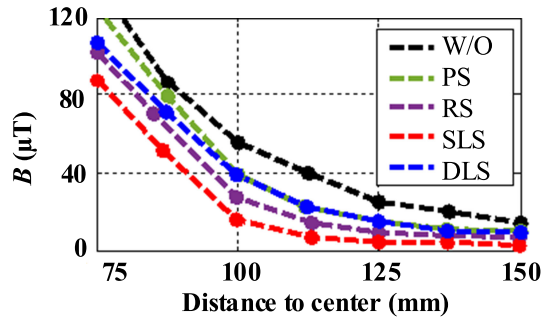

Fig. 14. Quantified stray magnetic fields from measurement along *Y*-axis, with the distance to the center ranging from 75 to 150 mm in Fig. 1(b).

Y-axis. The stray magnetic field is attenuated effectively with shorted litz shield.

VI. Conclusion

Litz shield is used to attenuate the stray magnetic field around the inductive-power-transfer coils in this paper. Compared to the plate shield and ring shield, litz shield is able to attenuate the magnetic field with smaller shielding loss, because the shield current is more uniformly distributed. The increased weight due to the litz shield is negligible. Litz shields are categorized as shorted litz shield and driven litz shield. The circuit models with four coupled inductors are derived for both categories, from which the equivalent inductances, the equivalent resistances, the windings' currents, and the shields' currents are all analyzed and obtained. Pareto fronts are used to optimize the coil-to-coil efficiency and stray magnetic field. A fast method to get the Pareto fronts using the lumped-loop model is described. The efficiency and magnetic field are calculated with permeance matrices, current-to-field matrices, and turns vectors of the lumped-loop model. Only tens of simulations are needed in the entire optimization procedure, which is much faster than the conventional method that takes thousands of simulations. The coils with different structures of shields were fabricated and measured in experiment. Both calculation and measurement show that the shorted litz shield is most effective for field attenuation. With all the shields designed for the same efficiency, shorted litz shield attenuated the stray magnetic field by up to 65% compared to coils without metal shield, in an IPT system to transfer 100-W power across 40-mm gap.

References

[1] S. Y. R. Hui, W. Zhong, and C. K. Lee, "A critical review of recent progress in mid-range wireless power transfer," *IEEE Trans. Power Electron.*, vol. 29, no. 9, pp. 4500–4511, Sep. 2014.

[2] G. A. Covic and J. T. Boys, "Modern trends in inductive power transfer for transportation applications," *IEEE J. Emerg. Sel. Topics Power Electron.*, vol. 1, no. 1, pp. 28–41, Mar. 2013.

[3] S. Li and C. C. Mi, "Wireless power transfer for electric vehicle applications," *IEEE J. Emerg. Sel. Topics Power Electron.*, vol. 3, no. 1, pp. 4–17, Mar. 2015.

[4] C. Zheng *et al.*, "High-efficiency contactless power transfer system for electric vehicle battery charging application," *IEEE J. Emerg. Sel. Topics Power Electron.*, vol. 3, no. 1, pp. 65–74, Mar. 2015.

[5] R. Bosshard, J. Mühlethaler, J. W. Kolar, and I. Stevanović, "Optimized magnetic design for inductive power transfer coils," in *Proc. 28th Annu. IEEE Appl. Power Electron. Conf. Expo.*, Long Beach, CA, USA, 2013, pp. 1812–1819.

[6] J. Sallan, J. L. Villa, A. Llombart, and J. F. Sanz, "Optimal design of ICPT systems applied to electric vehicle battery charge," *IEEE Trans. Ind. Electron.*, vol. 56, no. 6, pp. 2140–2149, Jun. 2009.

[7] O. H. Stielau and G. A. Covic, "Design of loosely coupled inductive power transfer systems," in *Proc. Int. Conf. Power Syst. Technol.*, Perth, WA, USA, 2000, vol. 1, pp. 85–90.

[8] M. Lu and K. D. T. Ngo, "Systematic design of coils in series–series inductive power transfer for power transferability and efficiency," *IEEE Trans. Power Electron.*, vol. 33, no. 4, pp. 3333–3345, Apr. 2018.

[9] M. Lu and K. D. T. Ngo, "Sequential design for coils in series-series inductive power transfer using normalized parameters," in *Proc. IEEE PELS Workshop Emerg. Technol., Wireless Power*, Knoxville, TN, USA, 2016, pp. 1–6.

[10] W. Zhang, J. C. White, A. M. Abraham, and C. C. Mi, "Loosely coupled transformer structure and interoperability study for EV wireless charging systems," *IEEE Trans. Power Electron.*, vol. 30, no. 11, pp. 6356–6367, Nov. 2015.

[11] R. Chen *et al.*, "Analysis and parameters optimization of a contactless IPT system for EV charger," in *Proc. IEEE Appl. Power Electron. Conf. Expo.*, Fort Worth, TX, USA, 2014, pp. 1654–1661.

[12] M. Lu and K. D. T. Ngo, "Pareto fronts for coils' efficiency versus stray magnetic field in inductive power transfer," in *Proc. IEEE PELS Workshop Emerg. Technol., Wireless Power*, Knoxville, TN, USA, 2016, pp. 1–5.

[13] International Commission on Non-Ionizing Radiation Protection, "ICNIRP guidelines for limiting exposure to time-varying electric, magnetic and electromagnetic fields (1 Hz to 100 kHz)," *Health Phys.*, vol. 99, pp. 818–836, 2010.

[14] H. Kim *et al.*, "Design of magnetic shielding for reduction of magnetic near field from wireless power transfer system for electric vehicle," in *Proc. Int. Symp. Electromagn. Compat.*, Gothenburg, Sweden, 2014, pp. 53–58.

[15] M. Lu and K. D. T. Ngo, "A fast method to optimize efficiency and stray magnetic field for inductive-power-transfer coils using lumped-loops model," *IEEE Trans. Power Electron.*, vol. 33, no. 4, pp. 3065–3075, Apr. 2018.

[16] M. Lu and K. D. T. Ngo, "Attenuation of stray magnetic field in inductive power transfer by controlling phases of windings' currents," *IEEE Trans. Magn.*, vol. 53, no. 9, Sep. 2017, Art no. 8700408.
[17] K. Seonghwan, P. Hyun-Ho, K. Jonghoon, K. Jingook, and A. Seungyoung, "Design and analysis of a resonant reactive shield for a wireless power electric vehicle," *IEEE Trans. Microw. Theory Techn.*, vol. 62, no. 4, pp. 1057–1066, Apr. 2014.
[18] A. Seungyoung and K. Joungho, "Magnetic field design for high efficient and low EMF wireless power transfer in on-line electric vehicle," in *Proc. 5th Eur. Conf. Antennas Propag.*, 2011, pp. 3979–3982.
[19] S. Y. Choi, B. W. Gu, S. W. Lee, W. Y. Lee, J. Huh, and C. T. Rim, "Generalized active EMF cancel methods for wireless electric vehicles," *IEEE Trans. Power Electron.*, vol. 29, no. 11, pp. 5770–5783, Nov. 2014.
[20] T. Miyoshi, H. Omori, and G. Maeda, "Reduction of magnetic flux leakage from an induction heating range," *IEEE Trans. Ind. Electron.*, vol. IA-19, no. 4, pp. 491–497, Jul. 1983.
[21] M. Budhia, J. T. Boys, G. A. Covic, and C. Y. Huang, "Development of a single-sided flux magnetic coupler for electric vehicle IPT charging systems," *IEEE Trans. Ind. Electron.*, vol. 60, no. 1, pp. 318–328, Jan. 2013.
[22] M. Budhia, G. A. Covic, and J. T. Boys, "Design and optimization of circular magnetic structures for lumped inductive power transfer systems," *IEEE Trans. Power Electron.*, vol. 26, no. 11, pp. 3096–3108, Nov. 2011.
[23] R. Bosshard, J. W. Kolar, J. Muhlethaler, I. Stevanovic, B. Wunsch, and F. Canales, "Modeling and η-α-pareto optimization of inductive power transfer coils for electric vehicles," *IEEE J. Emerg. Sel. Topics Power Electron.*, vol. 3, no. 1, pp. 50–64, Mar. 2015.
[24] K. Jiseong *et al.*, "Coil design and shielding methods for a magnetic resonant wireless power transfer system," *Proc. IEEE*, vol. 101, no. 6, pp. 1332–1342, Jun. 2013.
[25] Y. H. Sohn, B. H. Choi, E. S. Lee, and C. T. Rim, "Comparisons of magnetic field shaping methods for ubiquitous wireless power transfer," in *Proc. IEEE PELS Workshop Emerg. Technol., Wireless Power*, Daejeon, South Korea, 2015, pp. 1–6.
[26] J. L. Villa, J. Sallan, J. F. Sanz Osorio, and A. Llombart, "High-misalignment tolerant compensation topology for ICPT systems," *IEEE Trans. Ind. Electron.*, vol. 59, no. 2, pp. 945–951, Feb. 2012.
[27] N. A. Keeling, G. A. Covic, and J. T. Boys, "A unity-power-factor IPT pickup for high-power applications," *IEEE Trans. Ind. Electron.*, vol. 57, no. 2, pp. 744–751, Feb. 2010.
[28] G. Buja, M. Bertoluzzo, and K. N. Mude, "Design and experimentation of WPT charger for electric city car," *IEEE Trans. Ind. Electron.*, vol. 62, no. 12, pp. 7436–7447, Dec. 2015.
[29] U. K. Madawala and D. J. Thrimawithana, "A bidirectional inductive power interface for electric vehicles in V2G systems," *IEEE Trans. Ind. Electron.*, vol. 58, no. 10, pp. 4789–4796, Oct. 2011.
[30] Y. Zhang, T. Lu, Z. Zhao, F. He, K. Chen, and L. Yuan, "Selective wireless power transfer to multiple loads using receivers of different resonant frequencies," *IEEE Trans. Power Electron.*, vol. 30, no. 11, pp. 6001–6005, Nov. 2015.
[31] L. Kibok, Z. Pantic, and S. M. Lukic, "Reflexive field containment in dynamic inductive power transfer systems," *IEEE Trans. Power Electron.*, vol. 29, no. 1, pp. 4592–4602, Sep. 2014.
[32] E. Waffenschmidt, "Homogeneous magnetic coupling for free positioning in an inductive wireless power system," *IEEE J. Emerg. Sel. Topics Power Electron.*, vol. 3, no. 1, pp. 226–233, Mar. 2015.
[33] J. A. Ferreira, "Improved analytical modeling of conductive losses in magnetic components," *IEEE Trans. Power Electron.*, vol. 9, no. 1, pp. 127–131, Jan. 1994.
[34] C. R. Sullivan, "Computationally efficient winding loss calculation with multiple windings, arbitrary waveforms, and two-dimensional or three-dimensional field geometry," *IEEE Trans. Power Electron.*, vol. 16, no. 1, pp. 142–150, Jan. 2001.
[35] M. Lu and K. D. T. Ngo, "An analytical method to calculate winding resistance for planar coil with ferrite plate and litz wire in inductive power transfer," in *Proc. IEEE Energy Convers. Congr. Expo.*, Cincinnati, OH, USA, 2017, pp. 111–117.
[36] I. Lope, J. Acero, and C. Carretero, "Analysis and optimization of the efficiency of induction heating applications with litz-wire planar and solenoidal coils," *IEEE Trans. Power Electron.*, vol. 31, no. 7, pp. 5089–5101, Jul. 2016.
[37] J. Mühlethaler, "Modeling and multi-objective optimization of inductive power components," Ph.D. dissertation, Dept. Inf. Technol. Electr. Eng., ETHZ Zürich, Zürich, Switzerland, 2012.

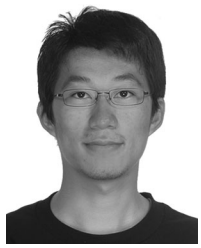

Ming Lu (S'16–M'18) received the B.S. and M.S. degrees in electrical engineering from Shanghai Jiao Tong University, Shanghai, China, in 2008 and 2012, respectively, and the Ph.D. degree in electrical engineering from Virginia Tech, Blacksburg, VA, USA, in 2017.

He is currently a Senior Applications Engineer with Monolithic Power Systems Inc., San Jose, CA, USA. His research interests include wireless power transfer, wide bandgap power semiconductor devices, and dc–dc power conversion.

Khai D. T. Ngo (S'82–M'84–SM'02–F'15) received the B.S. degree in electrical and electronics engineering from California State Polytechnic University, Pomona, CA, USA, in 1979, and the M.S. and Ph.D. degrees in electrical and electronics engineering from the California Institute of Technology, Pasadena, CA, in 1980 and 1984, respectively.

He was a Member of Technical Staff with General Electric Corporate Research and Development Center, Schenectady, NY, USA, from 1984 to 1988. Between 1988 and 2006, he was with the University of Florida, Gainesville, USA. He is currently a Professor of electrical and computer engineering with Virginia Tech, Blacksburg, VA, USA. At Virginia Tech, he pursues technologies for integration and packaging of power passive and active components to realize building blocks for power electronic systems. These technologies lead to power conversion systems with higher efficiency and higher power density. His research interests include topologies, control, emission, and integration issues for RF power converters. Other research interests include magnetic materials and components, energy reclamation, and power-integrated circuits.